Morphology changes in the evolution of liquid two-layer films

Andrey Pototsky,[a] Michael Bestehorn, and Domnic Merkt
Lehrstuhl für Theoretische Physik II, Brandenburgische Technische Universität Cottbus, Erich-Weinert-Straße 1, Cottbus D-03046, Germany

Uwe Thiele
Max-Planck-Institut für Physik komplexer Systeme, Nöthnitzer Straße 38, Dresden D-01187, Germany

(Received 26 January 2005; accepted 13 April 2005; published online 16 June 2005)

We consider a thin film consisting of two layers of immiscible liquids on a solid horizontal (heated) substrate. Both the free liquid–liquid and the liquid–gas interface of such a bilayer liquid film may be unstable due to effective molecular interactions relevant for ultrathin layers below 100-nm thickness, or due to temperature-gradient-caused Marangoni flows in the heated case. Using a long-wave approximation, we derive coupled evolution equations for the interface profiles for the general nonisothermal situation allowing for slip at the substrate. Linear and nonlinear analyses of the short- and long-time film evolution are performed for isothermal ultrathin layers, taking into account destabilizing long-range and stabilizing short-range molecular interactions. It is shown that the initial instability can be of a varicose, zigzag, or mixed type. However, in the nonlinear stage of the evolution the mode type, and therefore the pattern morphology, can change via switching between two different branches of stationary solutions or via coarsening along a single branch.
 [DOI: 10.1063/1.1927512]

I. INTRODUCTION

Instabilities of thin liquid films between a solid substrate and a gas atmosphere have attracted much scientific interest. The main focus lies thereby on front instabilities of moving contact lines or on instabilities of the free liquid–gas interface of a flat film. A recent review can be found in Ref. 1. To analyze such instabilities a long-wave or lubrication approximation[1–3] is often used as a very powerful tool especially for low Reynolds number film flows. At present the basic behavior of one-layer films in the physically different thickness ranges is well understood. Several instability mechanisms exist that, by means of different driving forces, may destabilize an initially flat film. They are described, analyzed, and modeled in a large number of experimental[4–7] and theoretical[8–16] works.

For film thicknesses d less than about 100 nm, effective molecular interactions between the film surface and the substrate dominate all the other forces, like thermocapillarity, and solutocapillarity or gravity, and thus determine the film stability.[17–19] For heated films of thicknesses above 100 nm, thermocapillary forces eventually become dominant, leading to an instability caused by large-scale Marangoni convection.[5,20,21] It dominates below a limiting film thickness determined by the competition between large-scale and small-scale convection modes.[22] For even thicker films with $d > 100$ μm gravity also becomes important. Depending on its direction it may stabilize the large-scale Marangoni instability or destabilize the film further (Rayleigh–Taylor instability).[10,23] For the latter, the lubrication approximation is valid up to a limiting film thickness of about 10^2 to 10^3 μm.

The effective molecular interactions that determine the stability and evolution of ultrathin liquid films with $d < 100$ nm arises, for instance, from long-range van der Waals and short-range electrostatic or entropic interactions.[24] Flat films are linearly unstable if the energy of the intermolecular interaction is a convex function of the film thickness. For ultrathin film thicknesses above 10 nm the van der Waals interactions dominate. The stability of a film may change dramatically for a substrate coated with a layer of different dielectric properties as, for instance, a silicon substrate (Si) coated with a silicon oxide layer (SiO).[7] There, for an oxide layer of about 2 nm only polystyrene (PS) films with below 4 nm thickness are linearly unstable. The critical thickness of the PS film can be controlled by the thickness of the oxide layer.

Imagine one replaces the (solid) coating layer by a liquid layer transforming the system into a two-layer liquid film. Some of the results obtained for a solid coating can directly be transferred to the new situation. The stability of the (now) upper layer still depends on the (now) liquid coating layer. However, additionally the liquid coating layer itself may be unstable leading to different instability modes. This thought experiment leads us beyond the well-studied one-layer systems to two-layer systems that are analyzed in the present work. In general, two possible two-layer geometries exist. The two liquid layers can be situated between two solid plates, leaving only the interface between the two liquids free to move. As a consequence, such a system can be described by a single evolution equation.[25,26] In contrast, the two layers can be situated between a solid substrate and a gas atmosphere. In this case the liquid–liquid and the liquid–gas interface can move and their evolution has to be described by coupled evolution equations. Models were derived, for instance, assuming a lower liquid layer that is much thicker

[a]Electronic mail: pototsky@physik.tu-cottbus.de

than the upper layer,[27] and for two-layer systems with surfactants (and non-Newtonian behavior)[28–30] or including evaporation.[31–33] A two-layer system under the sole influence of long-range molecular interactions is studied in Refs. 34–36.

The experimental interest in two-layer liquid films is, up to now, mainly focused on the dewetting of a liquid layer from a very thick lower layer or a liquid bulk substrate.[37–42] In contrast, Ref. 43 studies the dewetting of a polystyrene (PS) layer of 15 to 68 nm thickness from a 46 mm thick polyamide (PA) layer. The substrate is a silicon (Si) wafer covered with a layer of native oxide. At high temperature (195 °C) and small thicknesses (15–35 nm) the PS layer is unstable and dewets, exhibiting typical spinodal patterns. At low temperature (115 °C) the PA layer is solid resulting in a stable PS layer, independent of its thickness. This indicates the existence of two-layer instability modes that do not exist for the effective one-layer system at low temperature.

Recently, we presented a dynamical model for two-layer liquid films, taking into account long-range van der Waals interactions only.[36] Such a model allows for a study of pathways towards rupture but does not allow for a description of the long-time evolution of such films. In the present paper we present the derivation of film-thickness evolution equations for a general interaction energy and a nonisothermal situation. In the subsequent analysis of the short- and long-time evolution of two-layer liquid films the main focus lies on ultrathin layers with respective thicknesses below 100 nm, for which the effective molecular interactions between the four media are the dominant influence.

The paper is structured as follows. In Sec. II A we present the derivation of the long-wave evolution equations for a general nonisothermal case allowing also for slip at the substrate. The subsequent analysis focuses on the isothermal case without slip. Section III analyzes the linear stability of flat films starting from the general case in Sec. III A, then focusing on long-range van der Waals interactions in Sec. III B, discussing the possible mode types in Sec. III C, and introducing important limiting cases in Sec. III D. In Sec. IV we investigate the nonlinear behavior, discussing in Sec. IV A nonuniform stationary solutions as extrema of the Lyapunov functional, presenting in Sec. IV B two different pathways for mode changes in the course of the time evolution, and discussing long-time stationary solutions for different experimentally relevant systems in Sec. IV C. Concluding remarks follow in Sec. V. Expressions for the surface-tension gradients in terms of the gradients of the layer thicknesses are discussed in the Appendix.

II. DERIVATION OF COUPLED LARGE-AMPLITUDE EVOLUTION EQUATIONS

A. General case

First, we derive coupled evolution equations for the profiles of the liquid–liquid interface $h_1(x,y)$ and the liquid–gas interface $h_2(x,y)$. We assume that the layers are thin enough that convective terms can be neglected. Considering a two-dimensional geometry as sketched in Fig. 1, the respective Stokes equations for the two layers are

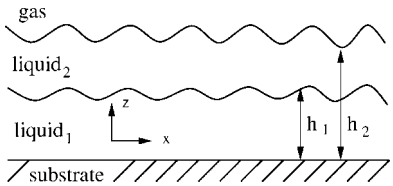

FIG. 1. Sketch of the problem in two dimensions. The local thickness of the lower layer is h_1; the total local film thickness is h_2.

$$\nabla(p_i + \phi_i) = \mu_i \Delta \boldsymbol{v}_i, \tag{1}$$

where $i=1,2$ denotes the respective layer. For each layer $\boldsymbol{v}_i=(u_i,w_i)$ is the velocity field, p_i is the pressure, ϕ_i is the potential of the bulk forces, and μ_i is the viscosity. The constant mean film thicknesses are denoted by $d_1=(\int_0^L h_1 dx)/L$ and $d_2=(\int_0^L h_2 dx)/L$, where L is the lateral system size. A lubrication approximation[1] is applied assuming the ratio of vertical and horizontal length scales to be small. As smallness parameter we use the ratio $\epsilon=d_1/\lambda$, where λ is the characteristic lateral length scale of the film instability. In zeroth order in ϵ Stokes Eq. (1) simplify to

$$\mu_2 \partial_z^2 u_2 = \partial_x \overline{p_2}, \tag{2}$$

$$\partial_z \overline{p_2} = 0, \tag{3}$$

$$\mu_1 \partial_z^2 u_1 = \partial_x \overline{p_1}, \tag{4}$$

$$\partial_z \overline{p_1} = 0, \tag{5}$$

where the $\overline{p_i}$ stand for $p_i+\phi_i$. At the substrate ($z=0$) we use a Navier slip and a no-penetration condition, i.e.,

$$u_1 = \beta \partial_z u_1 \quad \text{and } w_1 = 0, \tag{6}$$

respectively. The slip length is denoted by β. At the liquid–liquid interface ($z=h_1$) we use the continuity of the velocity field, the kinematic condition, and the continuity of the tangential component of the liquid stress tensor

$$u_1 = u_2, \tag{7}$$

$$w_1 = w_2, \tag{8}$$

$$w_1 = \partial_t h_1 + u_1 \partial_x h_1, \tag{9}$$

and

$$\mu_1 \partial_z u_1 - \mu_2 \partial_z u_2 = \partial_x \sigma_{12}, \tag{10}$$

respectively. The normal stress condition is discussed below. At the liquid–gas interface ($z=h_2$) only the kinematic condition and the continuity of the tangential component of the liquid stress tensor apply, i.e.,

$$w_2 = \partial_t h_2 + u_2 \partial_x h_2, \tag{11}$$

$$\mu_2 \partial_z u_2 = \partial_x \sigma_2. \tag{12}$$

The σ_{12} and σ_2 stand for the interfacial tensions of the liquid–liquid and of the liquid–gas interface, respectively. The boundary conditions for the normal component of the stress tensor are written, incorporating the disjoining pressures at the liquid–liquid $\Pi_1(h_1,h_2)$ and at the liquid–gas

$\Pi_2(h_1,h_2)$ interface, respectively. They represent effective molecular interactions between the interfaces that result, for instance, from van der Waals interactions.[24,44] They are discussed in detail below. For the liquid–gas interface ($z=h_2$) we obtain

$$p_2(h_2) - p_0 = -\sigma_2\partial_x^2 h_2 + \Pi_2(h_1,h_2),$$

and for the liquid–liquid interface ($z=h_1$)

$$p_1(h_1) - p_2(h_1) = -\sigma_{12}\partial_x^2 h_1 + \Pi_1(h_1,h_2), \tag{13}$$

where p_0 is the constant pressure in the gas atmosphere. Equation (13) can be written in terms of variations of an energy functional $F[h_1,h_2]$

$$p_1(h_1) - p_2(h_1) = \frac{\delta F}{\delta h_1},$$

$$p_2(h_2) - p_0 = \frac{\delta F}{\delta h_2}, \tag{14}$$

with

$$F = \int \left(\sigma_1 \frac{(\partial_x h_1)^2}{2} + \sigma_2 \frac{(\partial_x h_2)^2}{2} + f(h_1,h_2) \right) dx \tag{15}$$

and $f(h_1,h_2)$ being the free energy of the flat films per unit area.

Equations (2) and (4) are integrated three times with respect to z to obtain the stream functions Ψ_i, defined by $(w_i=-\partial_x\Psi_i, u_i=\partial_z\Psi_i)$. The six x-dependent integration constants are determined using the boundary conditions (6), (7), (10), and (12). Thus the velocity fields in the two layers are given by

$$u_1 = \frac{1}{\mu_1}(\partial_x\overline{p_1})\frac{z^2}{2} + \frac{1}{\mu_1}(z+\beta)K_1,$$

$$u_2 = \frac{1}{\mu_2}(\partial_x\overline{p_2})\frac{z^2}{2} + \frac{1}{\mu_2}K_2(z-h_1) - \frac{\partial_x\overline{p_2}}{\mu_2}\frac{h_1^2}{2} + u_1(h_1), \tag{16}$$

with $K_1 = K_2 + \partial_x\sigma_{12} + [(\partial_x\overline{p_2}) - (\partial_x\overline{p_1})]h_1$ and $K_2 = \partial_x\sigma_2 - (\partial_x\overline{p_2})h_2$.

The stream functions Ψ_i are related to the flow in the lower layer $\Gamma_1 = \int_0^{h_1} u_1 dz$ and to the one in the upper layer $\Gamma_2 = \int_{h_1}^{h_2} u_2 dz$ by $\Gamma_1 = \Psi_1(h_1)$ and $\Gamma_1 + \Gamma_2 = \Psi_2(h_2)$. Using the Ψ_i we rewrite Eqs. (8) and (11) to obtain the evolution equations for the two interface profiles

$$\partial_t h_1 + \partial_x[\Psi_1(h_1)] = 0, \tag{17}$$

$$\partial_t h_2 + \partial_x[\Psi_2(h_2)] = 0. \tag{18}$$

Written in terms of the energy functional they read

$$\partial_t h_1 = \partial_x\left[Q_{11}\partial_x\frac{\delta F}{\delta h_1} + Q_{12}\partial_x\frac{\delta F}{\delta h_2} - D_{11}\partial_x\sigma_{12} - D_{12}\partial_x\sigma_2 \right],$$

$$\partial_t h_2 = \partial_x\left[Q_{21}\partial_x\frac{\delta F}{\delta h_1} + Q_{22}\partial_x\frac{\delta F}{\delta h_2} - D_{21}\partial_x\sigma_{12} - D_{22}\partial_x\sigma_2 \right], \tag{19}$$

with the mobility matrices of the pressure terms

$$\boldsymbol{Q} = \frac{1}{\mu_1}\begin{pmatrix} \frac{h_1^3}{3} + \beta h_1^2, & \frac{h_1^2}{2}\left(h_2 - \frac{h_1}{3}\right) + \beta h_1 h_2 \\ \frac{h_1^2}{2}\left(h_2 - \frac{h_1}{3}\right) + \beta h_1 h_2, & \frac{(h_2-h_1)^3}{3}\left(\frac{\mu_1}{\mu_2} - 1\right) + \frac{h_2^3}{3} + \beta h_2^2 \end{pmatrix} \tag{20}$$

and of the tangential stress terms

$$\boldsymbol{D} = \frac{1}{\mu_1}\begin{pmatrix} \frac{h_1^2}{2} + \beta h_1, & \frac{h_1^2}{2} + \beta h_1 \\ h_1\left(h_2 - \frac{h_1}{2}\right) + \beta h_2, & \frac{\mu_1(h_2-h_1)^2}{2\mu_2} + h_1\left(h_2 - \frac{h_1}{2}\right) + \beta h_2 \end{pmatrix}, \tag{21}$$

respectively. Note that the mobility matrix $\boldsymbol{Q}$ is symmetric and all mobilities Q_{ik} and D_{ik} are positive. Dropping the terms representing the effective molecular interactions, Eq. (19) represent the fully nonlinear equivalent for the weakly nonlinear equations derived in Refs. 45 and 46. Assuming that the interfacial tensions are influenced by thermocapillarity only, one can express the derivatives $\partial_x\sigma_{12}$ and $\partial_x\sigma_2$ in terms of gradients of local thicknesses $\partial_x h_i$. This is done in the Appendix.

For isothermal ultrathin liquid films one has $(\partial_x\sigma_{12} = \partial_x\sigma_2 = 0)$. The situation is then relaxational (or variational), i.e., Eq. (19) possess a Lyapunov functional, namely, the energy functional F, which decreases monotonously in time as shown next. The total time derivative of the Lyapunov functional is $dF/dt = \int((\delta F/\delta h_1)\partial_t h_1 + (\delta F/\delta h_2)\partial_t h_2)dx$. Expressing $\partial_t h_i$ in Eq. (19) and using partial integration with periodic boundary conditions, one obtains

$$\frac{dF}{dt} = -\int \sum_{i,k} Q_{ik}\left(\partial_x\frac{\delta F}{\delta h_i}\right)\left(\partial_x\frac{\delta F}{\delta h_k}\right)dx. \tag{22}$$

Because

$$\det \mathbf{Q} = \frac{(h_2-h_1)^3 h_1^3}{9\mu_1\mu_2} + \frac{1}{12\mu_1^2} h_1^4 (h_2-h_1)^2 + \beta\left(\frac{h_1^3}{3\mu_1^2}(h_2-h_1)^2 + h_1^2 \frac{(h_2-h_1)^3}{3\mu_1\mu_2} \right) > 0 \qquad (23)$$

and $Q_{ii}>0$, the quadratic form in Eq. (22) is positive definite, implying $dF/dt<0$. The existence of F allows to identify the stationary solutions of Eq. (19) with the extrema of F. This will be used below in Sec. IV A.

B. The disjoining pressures $\Pi_i(h_1, h_2)$

In many important cases, as for instance, for polymer films on apolar substrates,[4,47] the interaction energy is mainly determined by its long-range apolar dispersion part. However, if the model only takes into account a destabilizing long-range interaction the time evolution definitively leads to rupture of the upper or lower layer,[36] making it impossible to study the long-time coarsening behavior. To be able to study the long-time evolution one has to include stabilizing short-range interactions[24,48] into the model. Although these are normally not included for films of thicknesses above 10 nm because they do not change the stability of flat films, also for such films they become important in the nonlinear stage of evolution when the local thicknesses become comparable to their interaction length.

The long-range part of the interaction energy for each pair of interfaces (see Fig. 1) resulting from dispersive van der Waals interactions is given by $A_{ijkl}/2\pi h^2$ (see Ref. 24), where A_{ijkl} is a (four-index) Hamaker constant which corresponds to the interaction between the interfaces i-j and k-l. Each index in A_{ijkl} can be one out of g, 1, 2, and s (denoting gas, liquid 1, liquid 2, and substrate, respectively). The four-index Hamaker constant is calculated using an equivalent of Eq. (11.13) of Ref. 24 that is based on the assumption that the main absorption frequencies of all involved media are about $\nu_e = 3\times 10^{15}$ Hz and that the zero-frequency contribution is negligible. One uses

$$A_{ijkl} \approx \frac{3h\nu_e}{8\sqrt{2}} \frac{(n_i^2-n_j^2)(n_l^2-n_k^2)}{(n_i^2+n_j^2)^{1/2}(n_l^2+n_k^2)^{1/2}[(n_i^2+n_j^2)^{1/2}+(n_l^2+n_k^2)^{1/2}]}, \qquad (24)$$

where n_i are the refractive indices of the media. The three-index Hamaker constants are given by

$$A_{ijk} = A_{ijjk}. \qquad (25)$$

The short-range forces which can be of an electrostatic or structural nature[9,49] decay exponentially with h. The electrostatic part results from the formation of diffuse electric double layers in the vicinity of interfaces involving polar liquids.[50,51] For films with thicknesses in the range of the Debye length the diffuse double layers at the two interfaces overlap, resulting in a repulsive or attractive force between the interfaces. The corresponding interaction energy between the interfaces s-1 and 1-2 is given by $S_1 \exp[(l_0-h_1)/l_1]$ and between the interfaces 1-2 and 2-g by $S_2 \exp[(l_0-(h_2-h_1))/l_2]$, where $l_0=0.158$ nm is the Born repulsion length, and l_1, $l_2 \sim 1-10$ nm are the interaction lengths of the short-range interactions.[48] Further on, we consider the two correlation lengths l_1 and l_2 to be equal and denote them by l. $S_1>0$ and $S_2>0$ are the short-range components of the total spreading coefficients. They are related to the lower layer on the substrate below a bulk of the upper liquid and to the upper layer on the lower film as substrate below the ambient gas, respectively. We do not take into account short-range interactions between interfaces s-1 and 2-g.

Collecting the long-range and the short-range forces, the disjoining pressures $\Pi_1(h_1,h_2)$ and $\Pi_2(h_1,h_2)$ are specified as

$$\Pi_1(h_1,h_2) = \frac{A_{21s}}{6\pi h_1^3} - \frac{A_{12g}}{6\pi(h_2-h_1)^3} - \frac{S_1}{l_1}\exp\left[\frac{l_0-h_1}{l_1}\right] + \frac{S_2}{l_2}\exp\left[\frac{l_0-(h_2-h_1)}{l_2}\right],$$

$$\Pi_2(h_1,h_2) = \frac{A_{12g}}{6\pi(h_2-h_1)^3} + \frac{A_{g21s}}{6\pi h_2^3} - \frac{S_2}{l_2}\exp\left[\frac{l_0-(h_2-h_1)}{l_2}\right]. \qquad (26)$$

To nondimensionalize Eq. (19) we scale the thicknesses with l, the lateral coordinate x with $\lambda = l(d_2-d_1)\sqrt{2\pi\sigma_1/|A_{12g}|}$, and time t with $\tau=(2\pi)^2\sigma_1\mu_1 l(d_2-d_1)^4/A_{12g}^2$. Then the scaled energy functional,

$$F = \int \left[\frac{1}{2}(\partial_x h_1)^2 + \frac{\sigma}{2}(\partial_x h_2)^2 - \frac{\overline{A}_{12g}}{6(h_2-h_1)^2} - \frac{\overline{A}_{21s}}{6h_1^2} - \frac{\overline{A}_{g21s}}{6h_2^2} + c_1(h_1-\overline{d}_1) + c_2(h_2-\overline{d}_2) + \overline{S}_1\exp(-h_1) + \overline{S}_2\exp(h_1-h_2)\right] dx, \qquad (27)$$

involves the scaled Hamaker constants $\overline{A}_{ijkl}=[(d_2-d_1)/l]^2 A_{ijkl}/|A_{12g}|$, spreading coefficients $\overline{S}_i = 2\pi[(d_2-d_1)]^2 S_i \exp(d_0/l)/|A_{12g}|$, and mean layer thicknesses $\overline{d}_i = d_i/l$. The c_i are Lagrangian multipliers that ensure mass

conservation for the two liquids. The corresponding energy scale is $|A_{12g}|/2\pi(d_2-d_1)^2$ and the ratios of the mean layer thicknesses, surface tensions, and viscosities are $d=d_2/d_1$, $\sigma=\sigma_2/\sigma_1$, and $\mu=\mu_2/\mu_1$, respectively. Further on, we denote the scaled variables using the same symbols as before; i.e., the scaled mean thicknesses are given by d_i and the local thicknesses by h_i. The nondimensional mobility matrices are obtained from Eqs. (20) and (21) by dropping the factor $1/\mu_1$ and replacing β by β/l.

III. LINEAR STABILITY

A. General stability of flat films

We start the analysis of our model for two-layer films by discussing the linear stability of flat films with $h_1(x)=d_1$ and $h_2(x)=d_2$. Equation (19) are linearized in $\epsilon \ll 1$ for small-amplitude disturbances $\epsilon\chi_i \exp(\gamma t)\exp(kx)$ for $i=1,2$, where k, γ, and $\boldsymbol{\chi}=(\chi,1)$ are the wave number, growth rate, and amplitudes of the disturbance, respectively. The dispersion relation $\gamma(k)$ is obtained by solving the resulting eigenvalue problem $(\boldsymbol{J}-\gamma\boldsymbol{I})\boldsymbol{\chi}=0$.

For the isothermal case [$\partial_x\sigma_{12}=\partial_x\sigma_2=0$ in Eqs. (19)], the corresponding *non-symmetric* Jacobi matrix $\boldsymbol{J}$ is given by $\boldsymbol{J}=-k^2\boldsymbol{Q}\cdot\boldsymbol{E}$, where $\boldsymbol{Q}$ is the scaled mobility matrix. $\boldsymbol{E}$ is the energy matrix

$$\boldsymbol{E}=\begin{pmatrix} \dfrac{\partial^2 f}{\partial h_1^2}+k^2, & \dfrac{\partial^2 f}{\partial h_1 \partial h_2} \\ \dfrac{\partial^2 f}{\partial h_1 \partial h_2}, & \dfrac{\partial^2 f}{\partial h_2^2}+\sigma k^2 \end{pmatrix}, \tag{28}$$

where $f(h_1,h_2)$ is the local part of the energy density from Eq. (27). This yields

$$\gamma=\frac{\mathrm{Tr}}{2}\pm\sqrt{\frac{\mathrm{Tr}^2}{4}-\mathrm{Det}}, \tag{29}$$

where $\mathrm{Tr}=-k^2[2Q_{12}E_{12}+Q_{11}E_{11}+Q_{22}E_{22}]$ and $\mathrm{Det}=k^4 \det\boldsymbol{Q}\det\boldsymbol{E}$ are the trace and the determinant of $\boldsymbol{J}$. Since $\det\boldsymbol{Q}\neq 0$, the eigenvalue problem can be written as the generalized eigenvalue problem $(k^2\boldsymbol{E}+\gamma\boldsymbol{Q}^{-1})\boldsymbol{\chi}=0$. Because $\boldsymbol{E}$ and $\boldsymbol{Q}^{-1}$ are both symmetric and $\boldsymbol{Q}^{-1}$ is positive definite, one can deduce that all eigenvalues γ are real,[52] as expected for a variational problem. In the nonisothermal case, the Jacobi matrix is given by $\boldsymbol{J}=-k^2(\boldsymbol{Q}\cdot\boldsymbol{E}-\boldsymbol{D}\cdot\boldsymbol{\Gamma})$, where $\boldsymbol{\Gamma}$ is a scaled matrix of coefficients for the Marangoni terms. It is defined in Sec. II A. Neither the matrix $\boldsymbol{D}$ nor $\boldsymbol{\Gamma}$ are symmetric. This leads to (in general) complex eigenvalues indicating the possibility of oscillating motion in the nonisothermal case.[45]

Going back to the isothermal case, an inspection of the generalized eigenvalue problem shows that the stability threshold is completely determined by the eigenvalues of $\boldsymbol{E}$. Since the surface-tension terms are always positive, the onset of the instability is always found for $k=0$; i.e., the system is linearly stable, independent of the wavelength of the disturbance, for

$$\det\boldsymbol{E}>0 \quad \text{and} \quad E_{11}>0 \quad \text{at} \quad k=0. \tag{30}$$

An instability sets in if at least one of the conditions (30) is violated. Then the flat two-layer film is unstable to disturbances with k larger than zero and smaller than the cutoff wave number

$$k_c^2=-\frac{1}{2}\left(\frac{\partial^2 f}{\partial h_1^2}+\frac{1}{\sigma}\frac{\partial^2 f}{\partial h_2^2}\right) \pm\sqrt{\frac{1}{4}\left(\frac{\partial^2 f}{\partial h_1^2}-\frac{1}{\sigma}\frac{\partial^2 f}{\partial h_2^2}\right)^2+\frac{1}{\sigma}\left(\frac{\partial^2 f}{\partial h_1 \partial h_2}\right)^2} \tag{31}$$

determined by the condition $\det\boldsymbol{E}(k_c)=0$.

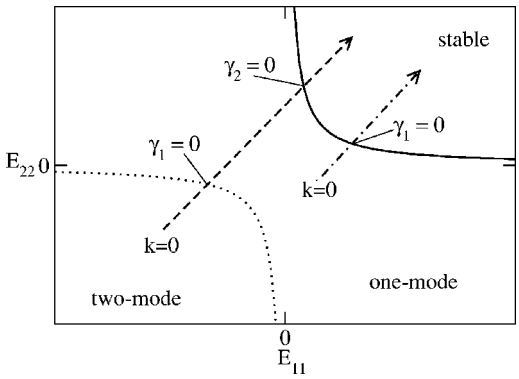

FIG. 2. The schematic stability diagram for fixed coupling E_{12}. Shown are the stability threshold (solid line) and the boundary between the one-mode and the two-mode region (dotted line). Both are given by $\det\boldsymbol{E}=0$ for increasing wave number k. Dashed and dot-dashed arrows represent parametric lines given by [$E_{11}(k)$ and $E_{22}(k)$]. The dashed (dot-dashed) line starts at $k=0$ in the two-mode (one-mode) region. At an intersection of a line $\det\boldsymbol{E}(k=0)$ and a parametric line one of the growth rates changes its sign.

Figure 2 shows a schematic stability diagram in the plane (E_{11},E_{22}). The stability threshold $E_{11}E_{22}=E_{12}^2$, $E_{11}>0$ is a hyperbola, represented by the solid line. The unstable region below and left of that line is divided by a second hyperbola into a two-mode and a one-mode region. In the two-mode region both growth rates given by Eq. (29) are positive for k smaller than the respective cutoff k_c. In the one-mode region only one γ is positive for $k<k_c$. Fixing all other system parameters, $\det\boldsymbol{E}(k)$ is determined by k. If at $k=0$ the system is in the two-mode region, then by increasing k one passes two times a line $\det\boldsymbol{E}=0$, as indicated by the dashed arrow in Fig. 2. At each crossing a growth rate [Eq. (29)] becomes negative; i.e., a mode is stabilized. If at $k=0$ the system is in the one-mode region the line $\det\boldsymbol{E}=0$ is crossed only once (dot-dashed line).

B. Long-range interaction only

To study the linear stability of layers with thicknesses of about 100 nm one can neglect the short-range terms in Eq. (27). In this case, Eq. (30) is used to study the role of the Hamaker constants [Eq. (24)] in the linear evolution of the system. First, we note that the Hamaker constants are coupled through the refractive indices of the media n_i. This allows only for selected combinations of signs of the A_{ijk} and A_{ijkl}, as given in Table I.

For fixed Hamaker constants, i.e., fixed combination of materials, $\det\boldsymbol{E}_0=\det\boldsymbol{E}(k=0)$ is a function of the ratio d of the layer thicknesses only. Using Table I, one can show that for positive $\partial^2 f/\partial h_i^2$ the equation $\det\boldsymbol{E}_0(d)=0$ can only have

TABLE I. Possible combinations of signs of the different Hamaker constants for a given order of the refractive indices of the involved media.

Refractive indices	A_{12g}	A_{21s}	A_{g21s}
$n_s>n_1$, $n_1<n_2$, $n_2>n_g$	+	+	−
$n_s<n_1$, $n_1<n_2$, $n_2>n_g$	+	−	+
$n_s<n_1$, $n_1>n_2$, $n_2>n_g$	−	+	+
$n_s>n_1$, $n_1>n_2$, $n_2>n_g$	−	−	−

the solution $d=1$, i.e., $d_2-d_1=0$. This means that only for vanishing upper layer the system can be on the stability threshold. As consequence, the stability threshold *cannot* be crossed by solely changing the ratio of layer thicknesses. This was analyzed in Ref. 36 for a variety of experimentally studied systems. Increasing the ratio d from one the system remains either completely in the unstable or in the stable region.

To compare the stability behavior of two-layer and one-layer films we introduce two effective one-layer films as follows. In case (1) we assume the lower layer to be solid; i.e., we regard the upper layer as a one-layer film on a coated substrate. In case (2) we assume the upper layer to be rigid but deformable by bending. The lower liquid layer corresponds then to a one-layer film on a solid bulk substrate. In case (1) the one-layer liquid film is unstable if the second derivative of the energy with respect to the film thickness h_2 is negative, $\partial^2 f/h_2^2<0$. The stability threshold at $\partial^2 f/h_2^2=0$ can be crossed by changing the layer thickness h_2-h_1 or the thickness of the coating layer h_1. This was demonstrated in Refs. 53 and 47 for a PS film on Si wafers covered with a 1.6-nm-thick SiO layer. In case (2) the one-layer liquid film is unstable for $\partial^2 f/h_1^2<0$. It can also be destabilized by changing the layer thicknesses, as was shown in Ref. 54 for a rigid PS layer on top of a liquid poly(dimethylsiloxane) (PDMS) layer on a Si substrate.

Comparing the stability thresholds for the two effective one-layer systems to the stability diagram in Fig. 2 shows that the stability threshold of the two-layer system lies in the region where both effective one-layer systems are stable. This indicates that a two-layer system is always less stable than the corresponding effective one-layer systems.

C. Different instability modes

The stability threshold can be studied in rather general terms as was done above because its main features do not depend on surface tensions or viscosities. However, this is not the case for the characteristics of the instability such as mode type, growth rates, or dominant wave length. To discuss these we focus in the following on selected two-layer films studied experimentally.[41,53,55] We consider various combinations of layers of polystyrene (PS), poly(methylmethacrylate) (PMMA) and poly(dimethylsiloxane) (PDMS) on a silicon (Si) or on a silicon oxide (SiO) substrate. The Hamaker constants for different combinations are calculated using Eq. (24) and given in Table II.

The linear instability of a two-layer film has two different modes. It can be of zigzag or varicose type. For the former the deflections of the two interfaces are in phase whereas for the latter they are in antiphase. For special parameter values one can also find a mixed type, where modes are present because they have equal fastest growth rates.[36]

TABLE II. Hamaker constants for various combinations of polymers.

System	$A_{12g}\times10^{-20}$ nm	$A_{21s}\times10^{-20}$ nm	$A_{g21s}\times10^{-20}$ nm
Si/PMMA/PS/air	1.49	3.8	−23.02
SiO/PMMA/PS/air	1.49	−0.024	0.15
SiO/PS/PDMS/air	−1.83	0.42	1.25

The model studied in Ref. 27 assumes a thick lower layer, thereby neglecting the interaction between the substrate and the liquid–liquid and liquid–gas interfaces. In this case only the varicose mode can be unstable. In the general case, however, also the zigzag mode can become unstable. Both modes are normally asymmetric; i.e., the deflection amplitudes of the two interfaces differ. We characterize this asymmetry by $\phi=\chi/(1+\chi^2)$. Negative (positive) ϕ corresponds to varicose (zigzag) modes. The value $|\phi|=1/2$ represents the symmetric case, whereas $\phi=0$ corresponds to maximal asymetry; i.e., one of the interfaces is flat. The asymmetry increases with the ratio of the surface tensions σ. Note that the dispersion relation and the type of the dominant mode depend on σ and μ, whereas the stability diagram in Fig. 2 *does not*.

The two mode types are plotted in Fig. 3 for a Si/PMMA/PS/air system for a fixed value of d and different ratios of viscosities μ. The dispersion relations $\gamma(k)$ are shown together with the corresponding ϕ. We show here that the type of the dominant mode can be changed by varying d or μ. It can also change in the dependence of the ratio of the interfacial tensions σ as studied in Ref. 36.

Strictly speaking, the concept of the mode type characterized by ϕ is only valid in the linear stage of the evolution. However, to discuss morphology changes we generalize this

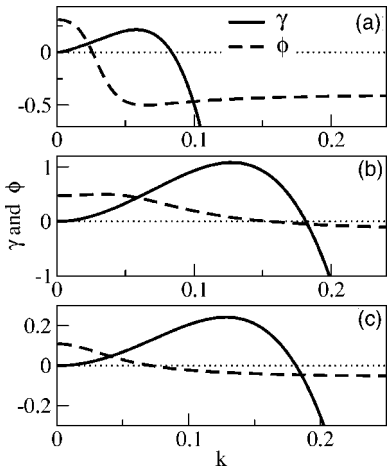

FIG. 3. Shown are the growth rate γ (solid lines) and the mode type ϕ (dashed lines) of the leading eigenmode. (a) A varicose mode from the one-mode region at $d_1=30, d_2=47$, and $\sigma=\mu=1$. (b) A zigzag mode from the one-mode region at $d_1=15$, $d_2=40$, and $\sigma=\mu=1$. Panel (c) gives γ and ϕ for d_1 and d_2 as in (b) but for $\mu=0.1$. For convenience we plot in (b) 10γ and in (a) 20γ.

concept to nonlinear thickness profiles $h_i(x)$. We define a generalized mode or solution type by the integral

$$\phi_{\text{int}} = \frac{1}{L}\int \frac{(h_1 - d_1)(h_2 - d_2)}{[(h_1 - d_1)^2 + (h_2 - d_2)^2]}dx, \tag{32}$$

taken over the domain length L. In many cases the sign of the product $(h_1-d_1)(h_2-d_2)$ does not depend on x allowing "to read" the mode type directly from the plots of the layer profiles. For small deflection amplitudes Eq. (32) gives again the linear mode type defined above. In the following we use the notion "mode type" in the linear and in the nonlinear regime.

D. Limiting cases

For general d_i the radical in Eq. (29) does not give an analytic expression for the wave number k_m and the characteristic growth time $\tau_m = 1/\gamma_{\text{m}}$ of the fastest growing mode. Nevertheless, one can derive asymptotic expressions for k_m and τ_m in the two important limiting cases of (1) small thickness of the upper layer $d_2 - d_1 \ll d_2$ and (2) small thickness of the lower layer $d_1 \ll d_2$. First, consider case (1), which corresponds to a liquid film (the upper layer) on a liquid substrate (the very thick lower layer). The dimensional k_m and τ_m are then given by

$$k_m = \frac{1}{(d_2 - d_1)^2}\sqrt{\frac{|A_{12g}|}{4\pi\sigma_{\text{eff}}}},$$

$$\tau_m = \frac{16(2\pi)^2\sigma_{\text{eff}}\mu_1(d_2 - d_1)^6}{d_1 A_{12g}^2}, \tag{33}$$

with $\sigma_{\text{eff}} = \sigma_1\sigma_2/(\sigma_1+\sigma_2)$. Note that all variables are in their dimensional form.

Interestingly, the growth time τ_m depends only on the viscosity of the lower layer μ_1 and does not depend on μ_2. This can be explained by the fact that the flow in the lower layer, which is related to μ_1, is much larger than that in the upper one.[27] At constant thickness of the lower layer, τ_m is proportional to $(d_2-d_1)^6$; i.e., a liquid film on a bulk liquid substrate evolves faster than the same film on a solid substrate [growth time $\sim(d_2-d_1)^5$] and even faster than the same film on a solid substrate with slippage (growth time $\sim(d_2-d_1)^5/[1+3\beta/(d_2-d_1)]$).

In case (2), which corresponds to a liquid film (the lower layer) on a solid substrate below the other liquid (the very thick upper layer), the dimensional k_m and τ_m are given by

$$k_m = \frac{1}{d_1^2}\sqrt{\frac{A_{21s}}{4\pi\sigma_1}},$$

$$\tau_m = \frac{12(2\pi)^2\sigma_1\mu_1 d_1^5}{A_{21s}^2}. \tag{34}$$

Note that in case (2) k_m and τ_m coincide with k_{low} and τ_{low}, respectively, the characteristics of the dominant mode of the instability of a liquid film below a bulk liquid calculated using one-layer theory. A discussion of this geometry for a Rayleigh–Taylor instability can be found in Refs. 23 and 56.

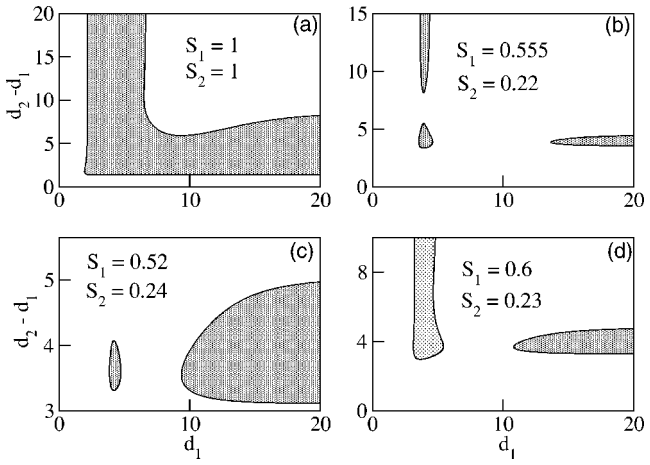

FIG. 4. Different types of stability diagrams in the plane of the layer thicknesses (d_1, d_2-d_1), shown for different strengths of the short-range interactions S_1 and S_2 as given in the legends. The shaded parts represent linearly stable regions. The Hamaker constants are $A_{12g}=1.49$, $A_{21s}=3.8$, and $A_{g21s}=-23.02$, corresponding to the Si/PMMA/PS/air system. Panels (a), (b), (c), and (d) correspond to ranges I, III, IV, and II in Fig. 5, respectively.

E. Long-range apolar and short-range polar interactions

The stability analysis based only on long-range interactions becomes incorrect for layer thicknesses in the range of the interaction length l of short-range interactions. Practically, the latter become important (well) below a 10-nm layer thickness. In contrast to the result for the exclusive action of long-range van der Waals forces, in the regime where both short- and long-range interactions are important the stability threshold can be crossed by changing the layer thicknesses d_i. Figure 4 presents a selection of qualitatively different stability diagrams in the plane spanned by the layer thicknesses obtained when varying the strength of the short-range interaction for a fixed long-range interaction.

By changing the short-range part of the spreading coefficients S_1 and S_2 one finds seven topologically different types of such diagrams. These types correspond to regions in the (S_1, S_2) plane as indicated in Fig. 5. In the absolute

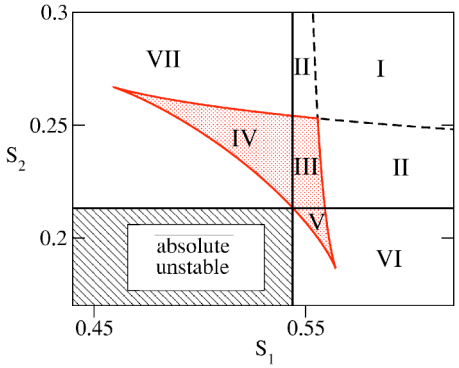

FIG. 5. Phase diagram in the plane (S_1, S_2) for the Si/PMMA/PS/air system. The absolute stable region (hatched rectangle in the lower left corner) is bounded by $(S_1)_{\text{min}} = (e/4)^4 A_{21s}/|A_{12g}|$ from the right and by $(S_2)_{\text{min}} = (e/4)^4$ from above. The unstable region is divided into seven qualitatively different subregions described in the main text.

unstable region bounded on the right by $(S_1)_{\min}=(e/4)^4 A_{21s}/|A_{12g}|$ and above by $(S_2)_{\min}=(e/4)^4$ the system cannot be stabilized by changing d_1 or d_2. Only if at least one of the two S_i is larger than the corresponding critical value (a) stable region(s) can be found in the (d_1, d_2-d_1) plane (see Fig. 4). For $S_1>(S_1)_{\min}$ a stable region exists that extends towards infinite (d_2-d_1), as shown in Figs. 4(a), 4(b), and 4(d). Thereby, for large (d_2-d_1) the system is stable for $(d_1)_{\min}<d_1<(d_1)_{\max}$, where $(d_1)_{\max}$ and $(d_1)_{\min}$ are the solutions of the equation $A_{21s}/|A_{12g}|=S_1 x^4 \exp(-x)$. Similarly, for $S_2>(S_2)_{\min}$ a stable region exists that extends towards infinite d_1, as in Figs. 4(a) to 4(d). For large d_1 the system is stable for $(d_2-d_1)_{\min}<d_2<(d_2-d_1)_{\max}$, where $(d_2-d_1)_{\max}$ and $(d_2-d_1)_{\min}$ are the solutions of Eq. (1) $=S_2 x^4 \exp(-x)$. In the gray shaded triangle at the center of Fig. 5 an additional bounded stable region exists in the (d_1, d_2-d_1) plane [see Figs. 4(b) and 4(c)]. Combining the different conditions gives the following seven types of stability diagrams.

(I) The stable region is continuous and extends in respective stripes towards infinite d_1 and d_2-d_1 [Fig. 4(a)].
(II) There exist two separated stable regions, one extending towards infinite d_1 and the other one towards infinite d_2-d_1 [Fig. 4(d)].
(III) Similar to type II but with an additional bounded stable region [Fig. 4(b)].
(IV) A bounded stable region exists together with an unbounded region extending towards infinite d_1 [Fig. 4(c)].
(V) Similar to type IV but with the unbounded region extending towards infinite (d_2-d_1) (not shown).
(VI) Only one stable region exists extending towards infinite d_1 (not shown).
(VII) Similar to type VI but with the unbounded region extending towards infinite (d_2-d_1) (not shown).

Further on, we will focus our attention on the stability diagram of type I.

IV. NONLINEAR BEHAVIOR

A. Stationary solutions as extrema of the Lyapunov functional

To find periodic stationary solutions of the scaled Eq. (19), the time derivatives $\partial_t h_i$ are set to zero. Integration yields

$$Q_{11}\partial_x\left(\frac{\delta F}{\delta h_1}\right)+Q_{12}\partial_x\left(\frac{\delta F}{\delta h_2}\right)=C_1,$$

$$Q_{21}\partial_x\left(\frac{\delta F}{\delta h_1}\right)+Q_{22}\partial_x\left(\frac{\delta F}{\delta h_2}\right)=C_2, \tag{35}$$

where C_i are constant and F is given by Eq. (27). Note that the left-hand sides of Eq. (35) represent the flow in the lower layer and the total flow, respectively. For a stationary state both flows are zero; i.e., the $C_1=C_2=0$. Because the mobility matrix $\boldsymbol{Q}$ is nonsingular, one concludes from Eq. (35) that the stationary states of Eq. (19) are the extrema of the Lyapunov functional F; i.e., they are solutions of

$$-\partial_{xx}h_1+\frac{\partial f}{\partial h_1}=c_1,$$

$$-\sigma\partial_{xx}h_2+\frac{\partial f}{\partial h_2}=c_2, \tag{36}$$

where f denotes the local part of Eq. (27) and the constant c_i correspond to the Lagrangian multipliers introduced in Sec. II A.

Note that Eq. (36) can be written as a four-dimensional dynamical system, i.e., a system of four first-order ordinary differential equations. Note, however, that because of the variational character of the two-layer problem the dynamical system is a Hamiltonian one (compare Refs. 19 and 57). This allows the use of the tools of dynamical systems theory in the analysis of the model. Film-thickness profiles of periodic arrays of droplets correspond then to periodic orbits in the four-dimensional phase space spanned by $(h_1, h_2, \partial_x h_1, \partial_x h_2)$. Fixed points of the dynamical system correspond to flat-film states. However, the stability of the flat-film solutions (in time) discussed above *does not* correspond to the stability of the fixed points of the dynamical system. The latter is related to the stability of a flat film in space that does not concern us here.

Modeling here nonvolatile liquids, we are interested in periodic solutions of fixed mean film thicknesses d_i. These can be obtained by continuation techniques[58–60] if one uses the chemical potentials c_i and the period of the solutions L as free continuation parameter. For volatile liquids near equilibrium one can also fix the c_i and use the mean film thicknesses as free continuation parameter. We start with analytically known stationary periodic small-amplitude profiles, which correspond to the linear eigenfunctions for the critical wave number k_c. We characterize the solutions by the deflection amplitudes A_1 and A_2, the energy E, the squared norm $L_2=(1/L)\int[(h_1-d_1)^2+(h_2-d_2)^2]dx$, and the integral mode type ϕ_{int}.

To determine the stability of the stationary solutions $h_i(x)$, we add small perturbations $\delta h_i(x)\sim\exp(\beta t)$ to both interfaces $h_i(x)$, linearize the full time-dependent evolution Eq. (19) around $h_i(x)$, and solve the obtained eigenvalue problem $\boldsymbol{L}(h_i, \partial_x h_i, \partial_x)\boldsymbol{\delta h}(x)=\beta\boldsymbol{\delta h}(x)$ for the linear operator $\boldsymbol{L}$ after discretizing it in space. The sign of the largest eigenvalue β determines the stability of the stationary solution. Note that due to the translational invariance of the evolution Eq. (19), there exists always a symmetry mode $\delta h_i(x)=\partial_x h_i(x)$ with the eigenvalue $\beta=0$.

B. Mode-type transitions

The type of the dominant instability mode calculated above by linear stability may not persist in the course of the nonlinear evolution. Possible mode-type changes may have a dramatic effect on the (observable) overall morphology of the film. We investigate these changes by studying both the evolution in time of the film profiles and the stationary solutions obtained by continuation.

The evolution in time is obtained by numerical simulations of the scaled coupled evolution equations [Eq. (19)] in

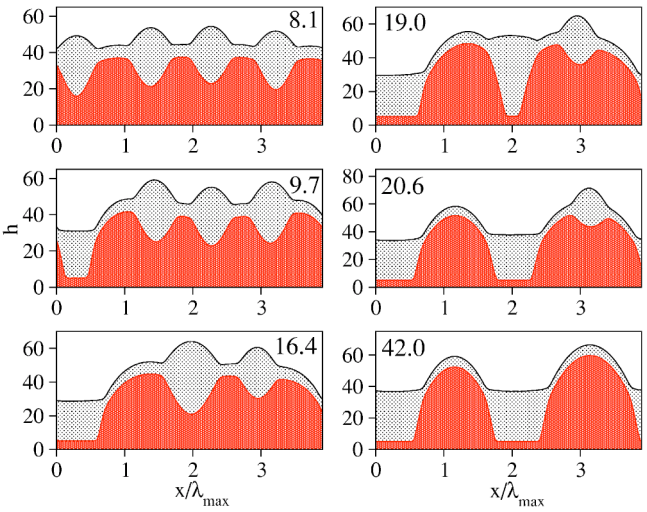

FIG. 6. Snapshots of the time evolution of a Si/PMMA/PS/air system for $d_1=30$, $d_2=47$, $S_1=S_2=1$, $\sigma=1$, and $\mu=1$ at times as given in the legends. The domain length is $L=4\lambda_m$ and time is in units of $1/\gamma_m$.

a one-dimensional periodic domain. Both semi-implicit pseudospectral and explicit time integration schemes are used. Initial conditions consist of flat layers with an imposed noise of amplitude 0.001.

1. Transition via branch switching

First, the time evolution of an initially flat film is studied for parameters as in Fig. 3(a) using a domain size equal to four times the fastest growing wave length λ_m. A time sequence of snap shots is shown in Fig. 6. In the early stage of the evolution a varicose mode develops ($t=8.1$), as expected from the linear analysis. Then in a subdomain of size λ_m the deflection amplitudes increase dramatically accompanied by a morphological change towards a zigzag-type profile ($t=9.7$). This is further illustrated by the dependence of the integral mode type [Eq. (32)] on time given in Fig. 7(b). Furthermore, the length of the zigzag part increases slightly and coarsening sets in, resulting in the disappearance of one varicose-type drop ($t=16.4$). Next, one of the remaining

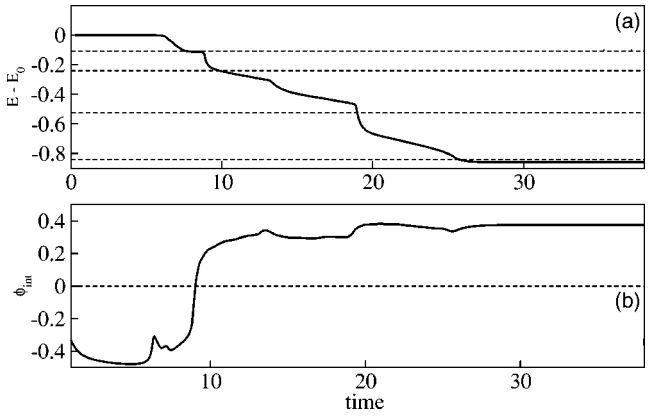

FIG. 7. Evolution in time of (a) the relative energy $E-E_0$ and (b) the integral mode type ϕ_{int} [Eq. (32)] for parameters as in Fig. 6. Time is in units of $1/\gamma_m$. In (a) the dashed lines denote the energy levels which correspond to the stationary solutions with periods $L=\lambda_m$ (first and second line from above), $L=4/3\lambda_m$ (third line from above), and $L=2\lambda_m$ (the lowest line) taken from Fig. 8(b).

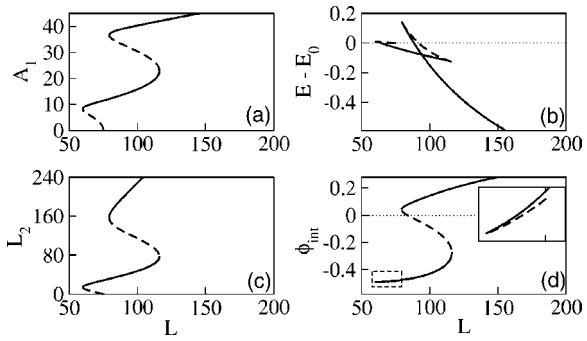

FIG. 8. Characterization of the stationary periodic solutions for the system of Fig. 7. Shown are (a) the amplitude of the lower layer A_1, (b) the relative energy $E-E_0$, (c) the squared norm L_2, and (d) the integral mode type ϕ_{int} in their dependence on the period L. In (d) the inset shows a zoom of the region marked by the dashed box.

drops increases its amplitude and flips to a zigzag-type hole ($t=20.6$). Finally, the last remaining varicose-type drop disappears ($t\approx 28$), and the system approaches a stationary (but not stable) state. The evolution of the relative energy of the profile in time is given in Fig. 7(a). It is seen very clearly that the phases of a very slow evolution correspond to solutions that are close to stationary solutions. This results from the fact that the (unstable) stationary solutions form saddle points in function space that are approached along their stable manifolds and subsequently repel the system along their unstable manifolds (for a discussion, see Ref. 61) The evolution stops after a further coarsening step, when the period becomes equal to the system size (not shown).

To explain the observed mode-type change, we study the stationary solutions of the evolution equations [Eq. (19)]. We find a family of solutions starting at the subcritical primary bifurcation, then turning three times at saddle-node bifurcations (folds) and going towards infinite periods [see Fig. 8(a)]. A stability analysis using the solution period as the period of the disturbance (thereby excluding coarsening modes) shows that two branches are stable (solid lines) and two are unstable (dashed lines). Along the first unstable branch, which starts at L_c and ends at the first fold at $L\approx 60$, the energy E is always larger than the one of the flat film E_0 [Fig. 8(b)], and it increases with decreasing period. This subcritical branch corresponds to nucleation solutions that have to be overcome to break the film in parts smaller than L_c (see Ref. 62 for a discussion of this type of solutions for a one-layer system). The first stable branch starts at the first fold at $L\approx 59$ and ends at the second fold at $L\approx 116$. Its relative energy decreases monotonically with increasing period. Mostly, it is energetically preferable to the flat film. The second unstable branch (between the second fold at $L\approx 116$ and the third fold at $L\approx 79$) turns back towards smaller periods. The second stable branch starts at the third fold and goes towards infinite periods. Its energy decreases rapidly from values even above the flat film to values below the ones of the first stable branch. The energy of the second unstable branch is always larger than the energies of both stable branches. This indicates that it corresponds to nucleation solutions, or critical solutions that have to be overcome to switch between the two stable branches. Along the second

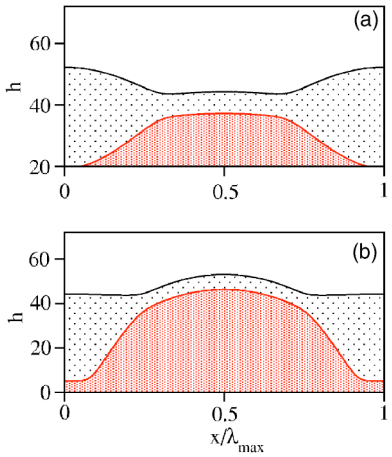

FIG. 9. The two stationary solutions with period $L=108.28$ (compare Fig. 8) corresponding to the wave length of the relevant dominant linear mode λ_{max}. Shown are (a) the varicose-type and (b) the zigzag-type solution from the first and second stable branch, respectively.

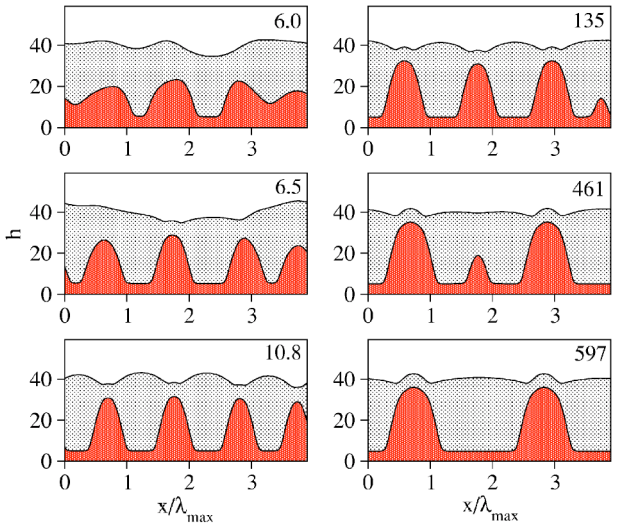

FIG. 10. Snapshots of the time evolution of a Si/PMMA/PS/air system for $d_1=15$, $d_2=40$, $S_1=S_2=1$, $\sigma=1$, and $\mu=1$ at times as given in the legends. The domain length is $L=4\lambda_m$ and time is in units of $1/\gamma_m$.

unstable branch, the mode-type changes from varicose to zigzag [Fig. 8(d)], explaining the nontrivial behavior observed in the time evolution shown in Fig. 6. There are two stable solutions with a period equal to the dominant linear wave length ($\lambda_m \approx 108$) (see Fig. 9). The one of higher energy that is approached first in the time evolution is of varicose type whereas the one of lower energy that the system switches to is of zigzag type [compare Fig. 8(b)]. A transition between the two solutions is accompanied by a strong increase of the amplitude A_1 [see Fig. 8(a)].

2. Transition via coarsening

A mode-type change is not always connected to a transition between different branches of stationary solutions. Also, coarsening along one branch may lead to such a change if the mode type varies along the branch. To demonstrate this, we simulate the time evolution using parameters as in Fig. 3(b). A time sequence of profiles and the corresponding evolution of the relative energy and the integral mode type are shown in Figs. 10 and 11, respectively. Early in the evolution, the layer profiles represent a zigzag mode ($t=6.0$) corresponding to the linear results [Fig. 3(b)]. Then, within the very short period of time from $t=6.0$ to 10.8, nonlinear effects result in a first change towards a varicose-type profile, as shown in the inset of Fig. 11(b). Then the system approaches the branch of stationary solutions. As a result, the evolution slows down and the pattern begins to coarse. With ongoing coarsening ($t>10.8$) the size of the droplets increases ($t=135, t=461$) and at very late times ($t>490$) the mode-type changes back to zigzag type [Fig. 11(b)]. Here, the amplitudes of the interfaces do not change dramatically, as was the case in Sec. IV B 1. In this sense the transition is continuous. The characteristics of the corresponding stationary solutions are shown in Fig. 12. The primary bifurcation is again subcritical [Fig. 12(a)]; the solution family continues towards smaller periods until turning at a saddle-node bifurcation (fold) and heading towards infinite periods. The subcritical branch is unstable with energies higher than the energy of the flat film [Fig. 12(b)]. The second branch starting at the fold ($L\approx 26$) consists of solutions, the energy of which decreases monotonically with increasing period. They are stable to disturbances of identical period but unstable to coarsening modes. Figure 12(d) shows that the solution with the period equal to $\lambda_m=50.81$ is of varicose type. The corresponding layer profile is shown in Fig. 13(a) together with the profile after the first coarsening step. When the period becomes larger than 94.2, the solution changes to zigzag type [Fig. 12(d)], as shown in Fig. 13(b). This explains the mode-type change found in the time evolution (Fig. 10).

Here we have restricted our attention to a parameter set corresponding to region I of Fig. 5, i.e., corresponding to the stability diagram shown in Fig. 4(a). The existence of a stable branch of stationary solutions which continues towards infinite period implies that the rupture of the two layers is completely avoided by the short-range repulsion. How-

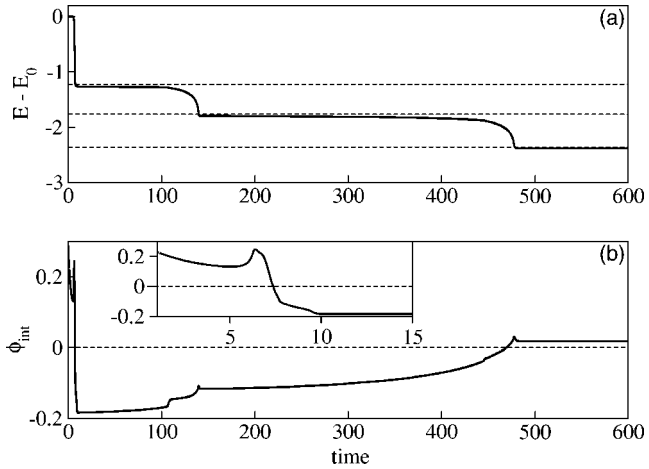

FIG. 11. Evolution in time of (a) the relative energy $E-E_0$ and (b) the integral mode type ϕ_{int} [Eq. (32)] for parameters as in Fig. 10. The inset in (b) shows the early-time behavior of the mode type. Time is in units of $1/\gamma_m$. In (a) the dashed lines denote the energy levels which correspond to the stationary solutions with periods $L=\lambda_m$, $L=4/3\lambda_m$, and $L=2\lambda_m$ taken from Fig. 12(b).

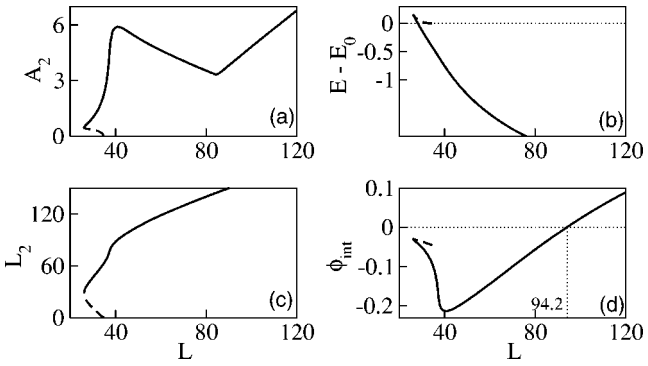

FIG. 12. Characterization of the stationary periodic solutions for the system of Fig. 10. Shown are (a) the amplitude of the upper layer A_2, (b) the relative energy $E-E_0$, (c) the squared norm L_2, and (d) the integral mode type ϕ_{int} in their dependence on the period L.

ever, this may not be the case for parameter ranges belonging to the other types of stability diagrams. A detailed analysis of the stationary solutions for all types will be done elsewhere.

C. Large-period stationary solutions

The stability of the numerical code, used to solve the evolution equations [Eq. (19)], requires a very small time step $t=0.00001$. As a result it takes very long even to reach the final stationary solution in a system of size $4\lambda_m$ using 256 grid points. It is not feasible at the moment to study many coarsening steps in this way. However, one can rely on continuation techniques that use an adaptive spatial grid along the continuation path[60] to obtain stationary solutions of arbitrarily large periods that correspond to solutions that would be obtained in a time evolution at very late times. We show in Fig. 14 possible large-period stationary solutions for different physical systems that are investigated experimentally. One finds qualitatively different morphologies like a drop of the lower liquid "looking through" a nearly flat film of the upper layer for a Si/PMMA/PS/air system. Note, however, that the upper layer is also continuous (due to the stabilizing short-range interaction), i.e., the drop is also covered by a very thin layer of the upper liquid. This is more pronounced for a SiO/PS/PDMS/air system. In contrast, for a SiO/PMMA/PS/air system one finds a drop of the upper liquid "swimming" on the lower liquid that is, however, attracted towards the base of the drop. These equilibrium solutions are equivalents of drop configurations studied in Ref. 63 for macroscopic (but smaller than the capillary length) drops. However, here the mesoscopic contact angles are not given explicitly but result from the underlying effective molecular interactions, i.e., the short- and long-range forces used.

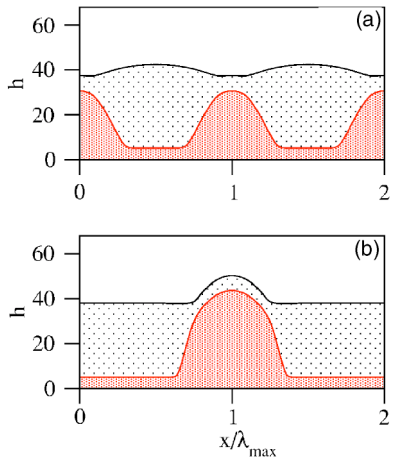

FIG. 13. The two stationary solutions with period $L=50.8$ and $L=101.6$ (compare Fig. 12) corresponding to once and twice the wave length of the dominant linear mode λ_{max}, respectively. To symbolize the coarsening process we show in (a) and (b) two and one period(s), respectively. The x coordinate is in units of λ_{max}.

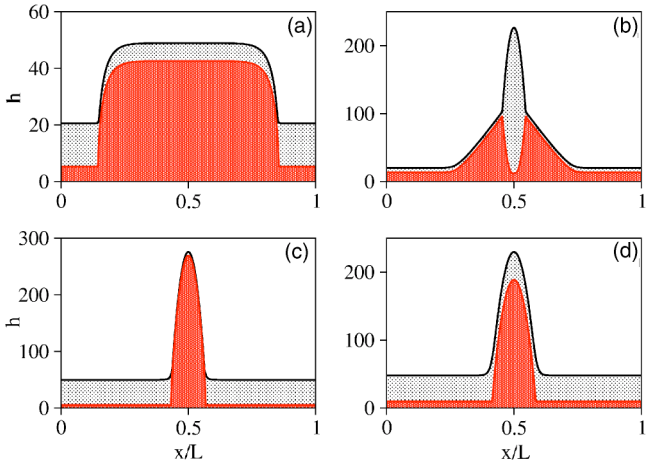

FIG. 14. Large-period (long-time) stationary profiles for (a) a Si/PMMA/PS/air system with $d_1=30$, $d_2=39$, $\lambda_m=132$, and period $L=26\times\lambda_m$; (b) a SiO/PMMA/PS/air with $d_1=30$, $d_2=50$, $\lambda_m=246$, and period $L=20\times\lambda_m$; (c) a Si/PMMA/PS/air system with $d_1=30$, $d_2=70$, $\lambda_m=118$, and $L=21\times\lambda_m$; and (d) a SiO/PS/PDMS/air with $d_1=30$, $d_2=70$, $\lambda_m=557$, and $L=10\times\lambda_m$. The remaining parameters are $\sigma=1$, $\mu=1$, and $S_1=S_2=1$.

V. CONCLUSION

We have derived coupled nonlinear evolution equations for the profiles of the liquid–liquid and liquid–gas interfaces of a thin two-layer liquid film heated from below, allowing for slip at the substrate. We have shown that in the isothermal case the evolution equations can be written in terms of variations of an appropriate Lyapunov functional F which monotonically decreases in time. The stability conditions for flat layers have been given in terms of F. We have shown that a two-layer film is less stable than related effective one-layer films introduced in Sec. III B. Even if both effective one-layer films are stable, the two-layer film may be unstable if the determinant of the energy matrix $\det \boldsymbol{E}$ is negative.

We have shown that if the Hamaker constants are given by the usual expression [Eq. (24)], i.e., they are coupled through the refractive indices, and no other forces are present, the stability of the flat films with thicknesses of ($\sim$100 nm) cannot be changed by solely changing the layer thicknesses. Incorporating a stabilizing short-range interaction, the stability can be changed in this way. We have

classified the resulting possible types of stability diagrams in the space of the layer thicknesses and given a "phase diagram" in terms of the short-range parts of the spreading coefficients for the occurrence of the different types of stability diagrams.

In general, the linear stability analysis of the flat film has shown that both varicose or zigzag mode may be unstable, depending on the ratios of the layer thicknesses, viscosities, and surface tensions (see also Ref. 36). This seems to be in contrast to Ref. 27. However, the difference arises because there it is assumed that the lower layer is thick compared to the upper layer, thereby neglecting all interactions with the substrate. Then the zigzag mode is always stable.

The introduction of the stabilizing short-range interaction allows for a study of the long-time evolution and stationary layer profiles. Possible stationary states have then been determined as extrema of the Lyapunov functional F. The resulting bifurcation diagrams show a rich branch structure that depends strongly on parameter values. We have focused on one type of stability diagram where a stable branch going towards infinite period always exists. This implies the existence of a nonruptured stationary state in the long-time limit also in the time evolution.

We have found that the mode type of a profile may change during the evolution of an instability in three ways. First, the profile-type changes in the course of the short-time evolution. This is connected to different mode types found for the dominant linear mode and the stationary solution of equal period in the solution branch approached first in the time evolution. It seems that this behavior is more probable for a subcritical primary bifurcation. In the case studied here this change is from zigzag to varicose. In the nonlinear regime the profile can change its type by (i) jumping from one to another stable branch and by (ii) coarsening along a single stable branch. Combinations of the different ways may also be possible. We have found that for the parameters considered here both nonlinear transitions go from varicose towards zigzag type. In case (i) the transition occurs without change of the period but with a dramatic increase in the amplitude of the profile. In case (ii) the transition occurs continuously without amplitude jump because mediated by coarsening a small-period varicose mode that turns into a large-period zigzag one.

In all examples considered here (except the SiO/PMMA/PS/air system with $d_1=30$, $d_2=50$) we have found a zigzag-type solution at large periods. For the future it would be very interesting to further analyze the stationary solutions for a broader range of experimentally interesting systems like the ones studied in Refs. 42 and 53. This should clarify under which conditions the zigzag type (or large-period) solutions are energetically preferable and determine how "late" the transition may occur. A systematic analysis of all types of stability diagrams would also discuss metastability and absolute stability of the flat two-layer films. Furthermore, we are very optimistic that the evolution equations presented here will serve to study the questions of hole growth and possible front instabilities in the dewetting of a liquid layer on a liquid substrate of finite thickness.[40,42]

ACKNOWLEDGMENTS

One of the authors (U.T.) acknowledges support through the EU RTN "Unifying principles in non-equilibrium pattern formation" (Contract MRTN-CT-2004–005728).

APPENDIX: TERMS $\partial_x\sigma_{12}$, $\partial_x\sigma_2$ IN NON-ISOTHERMAL CASE

To further specify the thermo-capillarity part of Eq. (19) we rewrite the derivatives $\partial_x\sigma_{12}$ and $\partial_x\sigma_2$ in terms of the gradients of the local thicknesses $\partial_x h_i$. In the long-wave approximation[1] the temperature field is in both layers a linear function of the vertical coordinate z, i.e., $T_i=a_i z+b_i$. To determine the coefficients we consider a three-layer geometry (Fig. 15), i.e., we take into account the heat conduction in a gas layer of finite thickness $d_g=d_t-d_2$, where d_t is the distance between the substrate and an upper plate. The temperature in the gas layer is $T_g=a_g z+b_g$. The boundary conditions at both interfaces are continuity of the temperature field and continuity of the heat flux $\kappa_i\partial_z T_i=\kappa_k\partial_z T_k$, where κ_i is the thermal conductivity of the ith layer. The temperatures at the substrate T_0 and at the upper plate T_t are constant. The coefficients a_i and b_i depend on the local thicknesses h_i and are given by

$$a_g=\frac{\alpha\Delta T}{d_t-h_2+\frac{\kappa_g}{\kappa_1}h_1+\frac{\kappa_g}{\kappa_2}(h_2-h_1)},$$

$$a_2=\frac{a_g\kappa_g}{\kappa_2},\quad a_1=\frac{a_g\kappa_g}{\kappa_1},$$

$$b_1=T_0,\quad b_g=T_t-a_g d_t,$$

$$b_2=a_g\kappa_g h_1\left(\frac{1}{\kappa_1}-\frac{1}{\kappa_2}\right)+T_0,$$

where $\Delta T=T_0-T_2$ and

$$\alpha=\frac{d_2-d_t-\kappa_g h_1/\kappa_1-\kappa_g(d_2-d_1)/\kappa_2}{\kappa_g h_1/\kappa_1-\kappa_g(d_2-d_1)/\kappa_2}.$$

Here T_2 is the temperature of the liquid–gas interface, when both interfaces are undeformed, i.e., for $h_i=d_i$. The above formulas allow the determination of the derivatives

$$\partial_x\sigma_{12}=\Gamma_{11}\partial_x h_1+\Gamma_{12}\partial_x h_2,$$

$$\partial_x\sigma_2=\Gamma_{21}\partial_x h_1+\Gamma_{22}\partial_x h_2, \tag{A1}$$

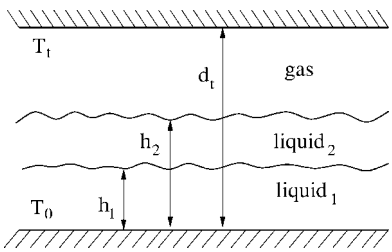

FIG. 15. Sketch of the system with a gas layer of finite thickness.

where the matrix $\mathbf{\Gamma}$ is determined as follows:

$$\mathbf{\Gamma} = a\begin{pmatrix} \frac{\kappa_g}{\kappa_1}\frac{d\sigma_1}{dT}b, & -\frac{\kappa_g}{\kappa_1}\frac{d\sigma_1}{dT}h_1\left(\frac{\kappa_g}{\kappa_2}-1\right) \\ \frac{d\sigma_2}{dT}\left(bc-\frac{\kappa_g}{\kappa_2}h_2 b\right), & \frac{d\sigma_2}{dT}\left\{\frac{\kappa_g}{\kappa_2}(d_t+h_1 b)-bh_1\left(\frac{\kappa_g}{\kappa_2}-1\right)\right\} \end{pmatrix}. \tag{A2}$$

Here $a=(\alpha\Delta T)/[d_t-h_2+\kappa_g/\kappa_1 h_1+\kappa_g/\kappa_2(h_2-h_1)]^2$, $b=\kappa_g(1/\kappa_1-1/\kappa_2)$, and $c=\{d_t-h_2(1-(\kappa_g/\kappa_2))\}$. For the linear normal Marangoni effect $d\sigma_{12}/dT$ and $d\sigma_2/dT$ are negative and constant. Equation (A2) is used in Eq. (19) to obtain a closed system of equations for h_1 and h_2.

[1] A. Oron, S. H. Davis, and S. G. Bankoff, Rev. Mod. Phys. **69**, 931 (1997).
[2] O. Reynolds, Philos. Trans. R. Soc. London **177**, 157 (1886).
[3] A. Sommerfeld, Z. Angew. Math. Phys. 50, 97 (1904).
[4] G. Reiter, Phys. Rev. Lett. **68**, 75 (1992).
[5] S. J. VanHook, M. F. Schatz, J. B. Swift, W. D. McCormick, and H. L. Swinney, J. Fluid Mech. **345**, 45 (1997).
[6] U. Thiele, M. Mertig, and W. Pompe, Phys. Rev. Lett. **80**, 2869 (1998).
[7] R. Seemann, S. Herminghaus, C. Neto, S. Schlagowski, D. Podzimek, R. Konrad, H. Mantz, and K. Jacobs, J. Phys.: Condens. Matter **17**, S267 (2005).
[8] M. B. Williams and S. H. Davis, J. Colloid Interface Sci. **90**, 220 (1982).
[9] P.-G. de Gennes, Rev. Mod. Phys. **57**, 827 (1985).
[10] A. Oron and P. Rosenau, J. Physique II France 2, 131 (1992).
[11] A. Sharma and R. Khanna, Phys. Rev. Lett. **81**, 3463 (1998).
[12] U. Thiele, M. G. Velarde, and K. Neuffer, Phys. Rev. Lett. **87**, 016104 (2001).
[13] E. Schäffer and U. Steiner, Eur. Phys. J. E **8**, 347 (2002).
[14] U. Thiele, Eur. Phys. J. E **12**, 409 (2003).
[15] A. L. Bertozzi, G. Grün, and T. P. Witelski, Nonlinearity **14**, 1569 (2001).
[16] A. Pototsky, M. Bestehorn, and U. Thiele, Physica D **199**, 138 (2004).
[17] E. Ruckenstein and R. K. Jain, J. Chem. Soc., Faraday Trans. 2 **70**, 132 (1974).
[18] A. Sharma, Langmuir **9**, 3580 (1993).
[19] V. S. Mitlin, J. Colloid Interface Sci. **156**, 491 (1993).
[20] M. Bestehorn, A. Pototsky, and U. Thiele, Eur. Phys. J. B **33**, 457 (2003).
[21] U. Thiele and E. Knobloch, Physica D **190**, 213 (2004).
[22] A. A. Golovin, A. A. Nepomnyashchy, and L. M. Pismen, Phys. Fluids **6**, 34 (1994).
[23] S. G. Yiantsios and B. G. Higgins, Phys. Fluids A **1**, 1484 (1989).
[24] J. N. Israelachvili, *Intermolecular and Surface Forces* (Academic, London, 1992).
[25] Z. Q. Lin, T. Kerle, T. P. Russell, E. Schäffer, and U. Steiner, Macromolecules **35**, 3971 (2002).
[26] D. Merkt, A. Pototsky, M. Bestehorn, and U. Thiele, Phys. Fluids **17**, 6 (2005).
[27] F. Brochard-Wyart, P. Martin, and C. Redon, Langmuir **9**, 3682 (1993).
[28] Y. L. Zhang, O. K. Matar, and R. V. Craster, J. Colloid Interface Sci. **262**, 130 (2003).
[29] R. V. Craster and O. K. Matar, J. Fluid Mech. **425**, 235 (2000).
[30] O. K. Matar, R. V. Craster, and M. R. E. Warner, J. Fluid Mech. **466**, 85 (2002).
[31] K. D. Danov, V. N. Paunov, N. Alleborn, H. Raszillier, and F. Durst, Chem. Eng. Sci. **53**, 2809 (1998).
[32] K. D. Danov, V. N. Paunov, S. D. Stoyanov, N. Alleborn, H. Raszillier, and F. Durst, Chem. Eng. Sci. **53**, 2823 (1998).
[33] V. N. Paunov, K. D. Danov, N. Alleborn, H. Raszillier, and F. Durst, Chem. Eng. Sci. **53**, 2839 (1998).
[34] D. Bandyopadhyay, R. Gulabani, and A. Sharma, Ind. Eng. Chem. Res. **44**, 1259 (2005).
[35] L. S. Fisher and A. A. Golovin (private communication).
[36] A. Pototsky, M. Bestehorn, D. Merkt, and U. Thiele, Phys. Rev. E **70**, 025201(R) (2004).
[37] P. Martin, A. Buguin, and F. Brochard-Wyart, Europhys. Lett. **28**, 421 (1994).
[38] O. Wunnicke, P. Müller-Buschbaum, M. Wolkenhauer, C. Lorenz-Haas, R. Cubitt, V. Leiner, and M. Stamm, Langmuir **19**, 8511 (2003).
[39] M. D. Morariu, E. Schäffer, and U. Steiner, Phys. Rev. Lett. **92**, 156102 (2004).
[40] A. Faldi, R. J. Composto, and K. I. Winey, Langmuir **11**, 4855 (1995).
[41] P. Lambooy, K. C. Phelan, O. Haugg, and G. Krausch, Phys. Rev. Lett. **76**, 1110 (1996).
[42] Q. Pan, K. I. Winey, H. H. Hu, and R. J. Composto, Langmuir **13**, 1758 (1997).
[43] C. Renger, P. Müller-Buschbaum, M. Stamm, and G. Hinrichsen, Macromolecules **33**, 8388 (2000).
[44] J. N. Israelachvili, Proc. R. Soc. London, Ser. A **331**, 39 (1972).
[45] A. A. Nepomnyashchy and I. B. Simanovskii, Prikl. Mat. Mekh. **54**, 593 (1990) [Appl. Math. Mech. **54**, 490 (1990)].
[46] A. A. Nepomnyashchy and I. B. Simanovskii, Q. J. Mech. Appl. Math. **50**, 149 (1997).
[47] R. Seemann, S. Herminghaus, and K. Jacobs, Phys. Rev. Lett. **86**, 5534 (2001).
[48] A. Sharma, Langmuir **9**, 861 (1993).
[49] G. F. Teletzke, H. T. Davis, and L. E. Scriven, Rev. Phys. Appl. **23**, 989 (1988).
[50] B. V. Derjaguin and L. D. Landau, Acta Physicochim. URSS **14**, 633 (1941).
[51] E. J. W. Verwey and J. T. G. Overbeck, *Theory of the Stability of Lyophilic Colloids* (Elsevier, Amsterdam, 1948).
[52] E. S. Manteuffel and K. Vetters, *Lineare Algebra* (Tuebner, Leipzig, 1972).
[53] M. D. Morariu, E. Schäffer, and U. Steiner, Eur. Phys. J. E **12**, 375 (2003).
[54] M. O. David, G. Reiter, T. Sitthai, and J. Schultz, Langmuir **14**, 5667 (1998).
[55] M. Sferrazza, C. Xiao, R. A. L. Jones, D. G. Bucknall, J. Webster, and J. Penfold, Phys. Rev. Lett. **78**, 3693 (1997).
[56] S. G. Yiantsios and B. G. Higgins, J. Colloid Interface Sci. **147**, 341 (1991).
[57] U. Thiele, M. G. Velarde, K. Neuffer, and Y. Pomeau, Phys. Rev. E **64**, 031602 (2001).
[58] E. Doedel, H. B. Keller, and J. P. Kernevez, Int. J. Bifurcation Chaos Appl. Sci. Eng. **1**, 493 (1991).
[59] E. Doedel, H. B. Keller, and J. P. Kernevez, Int. J. Bifurcation Chaos Appl. Sci. Eng. **1**, 745 (1991).
[60] E. Doedel, A. Champneys, T. Fairfrieve, Y. Kusnetzov, B. Sandstede, and X. Wang, *Continuation and Bifurcation Software for Ordinary Differential Equations* (Concordia University, Montreal, 1997).
[61] U. Thiele, L. Brusch, M. Bestehorn, and M. Bär, Eur. Phys. J. E **11**, 255 (2003).
[62] U. Thiele, K. Neuffer, Y. Pomeau, and M. G. Velarde, Colloids Surf., A **206**, 135 (2002).
[63] L. Mahadevan, M. Adda-Bedia, and Y. Pomeau, J. Fluid Mech. **451**, 411 (2002).